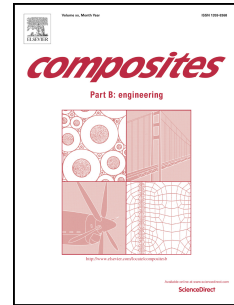


Accepted Manuscript

Combined ultrasonic-mechanical characterization of orthotropic elastic properties of an unrefined bagasse fiber-polypropylene composite

Thomas K. Bader, Foroogh Dastoorian, Ghanbar Ebrahimi, Gerhard Unger, Olaf Lahayne, Christian Hellmich, Bernhard Pichler



PII: S1359-8368(16)30158-5

DOI: [10.1016/j.compositesb.2016.03.070](https://doi.org/10.1016/j.compositesb.2016.03.070)

Reference: JCOMB 4171

To appear in: *Composites Part B*

Received Date: 11 June 2015

Revised Date: 21 March 2016

Accepted Date: 25 March 2016

Please cite this article as: Bader TK, Dastoorian F, Ebrahimi G, Unger G, Lahayne O, Hellmich C, Pichler B, Combined ultrasonic-mechanical characterization of orthotropic elastic properties of an unrefined bagasse fiber-polypropylene composite, *Composites Part B* (2016), doi: 10.1016/j.compositesb.2016.03.070.

This is a PDF file of an unedited manuscript that has been accepted for publication. As a service to our customers we are providing this early version of the manuscript. The manuscript will undergo copyediting, typesetting, and review of the resulting proof before it is published in its final form. Please note that during the production process errors may be discovered which could affect the content, and all legal disclaimers that apply to the journal pertain.

Combined ultrasonic-mechanical characterization of orthotropic elastic properties of an unrefined bagasse fiber-polypropylene composite

Thomas K. Bader^{a*}, Foroogh Dastoorian^{a,b}, Ghanbar Ebrahimi^b, Gerhard Unger^a,
Olaf Lahayne^a, Christian Hellmich^a, and Bernhard Pichler^a

^aInstitute for Mechanics of Materials and Structures, Vienna University of Technology (TU Wien),
Karlsplatz 13/202, A-1040 Vienna, Austria

^bUniversity of Tehran, P. O. Box 31585.3314, Karaj, Iran

*Corresponding author. E-mail address: thomas.bader@tuwien.ac.at; Tel.: +43 1 58801 20228

Abstract

Use of wood-fiber plastics for construction purposes calls for comprehensive understanding of their anisotropic mechanical properties. As a respective contribution, we here report the first-ever complete elasticity characterization of an orthotropic bagasse fiber polypropylene composite, requiring identification of nine independent constants. For this purpose, we carry out characterization in principal material directions. Six diagonal *stiffness* tensor components are quantified based on ultrasonic longitudinal and shear wave velocity measurements; and three diagonal *compliance* tensor components are identified as the inverses of three Young's moduli derived from unloading regimes of quasi-static uniaxial compression tests. Combination of all measurement data in the framework of orthotropic linear elasticity provides access to all off-diagonal stiffness and compliance tensor components, opening the door to quantifying six Poisson's ratios.

Keywords: A. Polymer-matrix composites (PMCs); B. Elasticity; B. Creep; D. Mechanical testing; D. Ultrasonics

1. Introduction

During sugar production, the extraction of cane juice from sugarcane delivers wooden fibers as by-product – they are called bagasse, and according to [1,2,3] consist of 40-50% cellulose, 25-35% hemicellulose, as well as of about 23.5% lignin, 1.3% ash, and 2.8% other components. Brazil, India, and China are the world's leading producers of the material, and they use bagasse typically for energy production by combustion. Other exploitation types include paper products, fiberboards, and fiber-polymer composites [4].

Cellulosic fibers are widely used for reinforcing purposes of all kind of matrix materials in order to enhance their mechanical properties, e.g. by reinforcing the material against brittle failure or reducing the creep activity of the composite [3,5]. Bagasse fiber polypropylene composites belong to the wide class of wood plastic composites (WPC). So far, WPCs have mainly been used for non-structural applications since the mechanical performance of WPCs is typically rather compliant, and exhibits a pronounced creep activity. However, recently developed technologies allow for the production of stiffer WPCs, thus opening the door to semi-structural applications, such as decking, railing, door and window profiles, siding, and roof tiles [6]. Recent feasibility studies investigate the potential use of WPCs for sill plates, deck substructure, and shoreline structures [7,8].

Verma et al. [4] reviewed research activities related to bagasse fiber composites and its constituents. Mechanical properties have mainly been measured in tensile and flexural tests following the protocols defined in major standards, such as ASTM D638, ASTM D747, ASTM D790-03, and ISO 527, see [9-11] for details. As regards the composite constituents, polypropylene is the “soft” matrix-type component with Young's modulus ranging from 0.9 to 1.3 GPa [1,5,9,10-14]; while bagasse plays the role of “reinforcing

fibers”, with Young’s modulus ranging from 2.7 to 4.5 GPa [14,15]. Accordingly, increasing bagasse contents increases the stiffness and strength of the overall plastic composites, as was shown in a number of experimental campaigns; see e.g. [9-17].

However, these experimental campaigns do not account for the anisotropic nature of bagasse fiber polypropylene composites [4,18], which results from the reorientation of originally randomly oriented fibers during the extruding process of a matrix-fiber composite [5,19]; and understanding of this anisotropic nature appears as essential for development of reliable design of, and improved production technologies for WPC elements. Assessment of the mechanical anisotropy of WPCs calls for largely increased experimental efforts, due to the increased number of independent material constants to be determined. In case of orthotropy, pure reliance on mechanical tests would require the measurement of deformations orthogonal to uniaxial loading directions coinciding with the material directions, plus subjecting the specimens to pure shear stresses. This would call for very elaborate testing equipment, which might still deliver unreliable results. As a remedy, we here resort to a combined mechanical-ultrasonic method in the line of [20]. This method circumvents the ultrasonic characterization of off-diagonal stiffness components which are very sensitive to inaccuracies regarding the measured wave velocities [20,21], and hence only employs measurements of ultrasonic longitudinal and shear wave velocities in all three orthotropic material directions, in order to obtain the six “diagonal” stiffness tensor components; i.e. those filling the diagonal in a 6x6 Kelvin-Mandel representation of stiffness tensors [22-24]. In addition, three Young’s moduli are measured in quasi-static uniaxial compression tests. Exploiting orthotropic symmetry, the aforementioned experimental dataset gives access to all nine independent elastic properties, and this allows

us to determine all Poisson's ratios. However, the quasi-static tests bear an additional challenge as compared to the original campaign on wood [20], in form of the very pronounced creep of the WPCs. Hence, utmost care has been devoted to the fact that elastic deformations should be measured in time scales where creep deformations have either not occurred to a remarkable degree yet, or have already largely faded away. This will be described in great detail in the section on mechanical tests, which is preceded by a description of the material and of the conducted ultrasonic tests. The paper is completed by a summary of the determined orthotropic elastic constants, and a few relevant conclusions.

2. Materials and Methods

2.1 Bagasse fiber-polypropylene composite specimens

Here, we characterize a bagasse fiber-polypropylene composite with a density of 1.1 g cm^{-3} , provided by the Iranian producer Dez choopex Co. The material consists of 60 wt% bagasse fibers (50 mesh size, i.e. 300 micrometer diameter according to [25]), 30 wt% polypropylene as polymer matrix, 4 wt% maleic anhydride polypropylene as compatibilizer, and 6 wt% other additives. The additives include UV stabilizers and lubricants, which improve the flowability and decrease the viscosity of the molten plastics. The raw materials were dry blended, and the composite was extruded using a counter rotating twin-screw-extruder combined with an I-shaped cross section die.

Light microscopic images of cross-sections parallel and normal to the extrusion direction were taken, in order to qualitatively visualize the size and the orientation of the bagasse fibers (Fig. 1). The length and width of the bagasse fibers typically amounted to $1000 \mu\text{m}$

and to 300 μm , respectively. In addition, bagasse fibers were quite well aligned with the extrusion direction (Fig. 1a).

Specimens for both ultrasonic and quasi-static tests were cut out from the web of the I-shaped profile (Fig. 2). For all computations performed in this paper, we use a Cartesian coordinate system to label the principal directions of the specimens: the x_1 -axis is aligned with the extrusion direction, the x_2 -axis points in thickness direction of the web, and the x_3 -axis runs in the web plane, normal to the extrusion direction (Fig. 2).

2.2 Ultrasonics testing

Ultrasonics experiments were carried out by means of a pulse transducer 5077PR - Olympus NDT, an oscilloscope WaveRunner 62Xi - Lecroy, and transducers with frequencies of 100 kHz and 250 kHz, respectively. Thin layers of honey ensured good contact between the pulse transducers and the investigated specimens. Nine samples with nominal dimensions of $51 \times 13 \times 13 \text{ mm}^3$ were insonified by both longitudinal and transversal ultrasonic waves (the former at a frequency of 100 kHz, and the latter at 250 kHz), in three orthogonal directions aligned with the three principal material directions (Fig. 2).

Homogenized material properties of microheterogeneous materials (such as ultrasound-derived elastic properties) are defined on representative volume elements (RVEs). They exhibit a characteristic size l_{rve} satisfying the separation of scales principle [26]: $\lambda \gg l_{rve} \gg d$, where d stands for the characteristic length of inhomogeneities inside the RVE, and where λ denotes the characteristic length of mechanical loading, which in case of ultrasonics testing, is equal to the wave length. Considering that the inequality $l_{rve} \gg d$ is typically satisfied (with maximum errors amounting to 5 %) if l_{rve} is by a factor of 2 larger

than d [27], the minimum RVE size l_{rve} amounts to 2 mm in extrusion direction, and to 0.6 mm normal to the extrusion direction. Considering that the inequality $\lambda \gg l_{rve}$ is typically satisfied if λ is by a factor of 6 larger than l_{rve} [28], the wavelength should be larger than 12 mm in extrusion direction, and larger than 3.6 mm normal to the extrusion direction. The wavelength λ , in turn, is readily accessible from the measured wave speed V and from the chosen signal frequency f as

$$\lambda = \frac{V}{f}. \quad (1)$$

The wave speed is equal to the travel distance s of the wave divided by the travel time t of the signal

$$V = \frac{s}{t}. \quad (2)$$

Each test was carried out nine times, allowing us to compute meaningful average values and standard deviations of ultrasonic wave travel times t , wave velocities V , and wavelengths λ (Table 1). For the sake of clarity, velocity symbols are marked with two indexes: the first index denotes the travel direction of the wave and the second index stands for the direction of particle displacements induced by the wave. In case of longitudinal waves, where the particle oscillation direction is parallel to the direction of wave propagation, both indexes are the same. In case of shear waves, where particles oscillate perpendicular to the wave propagation direction, the two indexes are different.

Stiffness tensor components can be computed from the mass density $\rho = 1.1 \text{ g cm}^{-3}$ of the composite, and the ultrasonic wave velocities, according to the theory of wave propagation in elastic media [29]

$$C_{iiii} = \rho V_{ii}^2, \quad (3)$$

and

$$C_{ijij} = \rho V_{ij}^2. \quad (4)$$

Accordingly, the normal stiffness tensor components C_{1111} , C_{2222} , and C_{3333} are related to longitudinal wave velocities V_{11} , V_{22} , and V_{33} ; while the shear stiffness components C_{1212} , C_{1313} , and C_{2323} , which are equal to the shear moduli G_{12} , G_{13} , and G_{23} , respectively, are related to transversal wave velocities V_{12} , V_{13} , and V_{23} .

2.3 Mechanical testing

Uniaxial, quasi-static mechanical testing in compression was carried out in all three principal material directions, using a universal electromechanical testing machine of type BT1-FB050TN of manufacturer Zwick/Roell. Rectangular specimens with nominal dimensions of $25 \times 13 \times 13 \text{ mm}^3$ and $13 \times 13 \times 25 \text{ mm}^3$ (directions $l_1 \times l_2 \times l_3$) were used for compression tests in directions x_1 and x_3 , while specimens with nominal dimensions of $6 \times 13 \times 6 \text{ mm}^3$ were used for measurements in direction x_2 , see Fig. 2. For each material direction, five replicates were tested.

Three step-like loading-unloading cycles with progressively increasing load levels were applied. In order to account for the different specimen dimensions, the corresponding compressive force levels were 0.8, 1.6, and 3.2 kN in directions x_1 and x_3 , and 0.2, 0.4, and 0.8 kN in direction x_2 . This resulted in comparable compressive stress levels applied in the different loading directions, namely amounting to 4.7, 9.5, and 18.9 N mm^{-2} in the x_1 and x_3 directions, as well as to 5.6, 11.1, and 22.2 N mm^{-2} in the x_2 direction. At each of the three load levels, the force was held constant for 600 s, in order to allow the initially significant creep activity to fade away. Subsequently, the compressive load was slightly reduced so as to determine unloading moduli. This accounts for the nature of elasticity as being related to

the mechanically recoverable energy stored in the loaded sample [30-32]. After the aforementioned slight unloading, the stresses were increased to a level exceeding the formerly applied one. Loading and unloading were carried out under displacement control, under consideration of the different specimen dimensions: In directions x_1 and x_3 , the loading and unloading rates were equal to 0.2 mm min^{-1} and 1 mm min^{-1} , respectively, while in direction x_2 , a loading rate of 0.1 mm min^{-1} and an unloading rate of 0.5 mm min^{-1} were prescribed. This resulted in comparable strain rates of 0.008 min^{-1} (loading) and 0.04 min^{-1} (unloading) for testing in directions x_1 and x_3 , and of 0.0077 min^{-1} (loading) and 0.0385 min^{-1} (unloading) in direction x_2 . Force and displacement readings were recorded at a data acquisition rate of 50 Hz. The Young's moduli in all three orthotropic material directions were determined from dividing the uniaxial stress rates measured at the beginning of the unloading regime, by the corresponding strain rate imposed in terms of the aforementioned displacement rates. In this context, it needs to be assured that corresponding stress rates reflect elastic deformations only, and do not contain remarkable contributions related to creep phenomena. Hence, creep deformations need to have sufficiently faded out before the unloading procedure starts. This requirement can be quantified in terms of a characteristic creep time T_{creep} and a characteristic time of strain evolution T_{evo} , namely the latter needs to significantly exceed the former, $T_{evo} \gg T_{creep}$. The characteristic creep time is obtained through a viscoelastic chain representation [33] of creep deformation histories under constant loads;

$$\varepsilon^{creep}(t) = \sigma_0 \sum_i^n A_i \left(1 - e^{-\frac{t}{\tau_i}}\right), \quad (5)$$

with t as the time elapsed since the application of the constant load given in terms of a uniaxial stress σ_0 , and with A_i and τ_i as amplitude and characteristic time characterizing the i -th viscoelastic chain element. n denotes the number of chain elements necessary to minimize the error between measurement data and creep predictions according to Eq. (5), to a value not exceeding a tolerated threshold value of $TOL = 10^{-7}$

$$\int_{t=1}^{600s} (\varepsilon^{exp}(t) - \varepsilon^{creep}(t))^2 dt = \sum_{t=1}^{600s} (\varepsilon^{exp}(t) - \varepsilon^{creep}(t))^2 < TOL. \quad (6)$$

The largest characteristic time τ_i in Eq. (5), stemming from minimization process in Eq. (6), is then identified as the time T_{creep} quantifying the duration of the overall creep process,

$$\tau_n = T_{creep}. \quad (7)$$

On the other hand, the characteristic time of strain evolution, T_{evo} , which indicates the degree of creep fade-out at the time of unloading, $t = t_{unload}$, follows the general definition of a characteristic time according to [34],

$$T_{def} = \frac{\varepsilon(t=t_{unload})}{\dot{\varepsilon}(t=t_{unload})}. \quad (8)$$

3. Results and Discussion

3.1 Ultrasonic testing

Ultrasonic wave velocities as measured for the bagasse-fiber composite, together with corresponding wave lengths, are reported in Table 1. The minimum longitudinal wave velocity was measured normal to the extrusion direction and amounted to $V_{22} = 1.83 \text{ km s}^{-1}$ (see Figure 2 for the definition of material directions). It was obtained with a signal frequency $f = 100 \text{ kHz}$. Hence, Eq. (1) implies that minimum longitudinal wavelength amounted to 18.3 mm, and this is larger than the required 3.6 mm. The minimum shear

wave velocity, in turn, amounted to $V_{32} = 1.06 \text{ km s}^{-1}$. It was obtained with a signal frequency $f = 250 \text{ kHz}$. Hence, Eq. (1) implies that minimum shear wavelength amounted to 4.24 mm, and this is larger than the required 3.6 mm. Hence, the separation-of scales requirement is fulfilled, and the measured velocities can be used to determine the elastic properties of the investigated composite.

Approximate identity of the ultrasonic shear wave velocities V_{ij} and V_{ji} (Table 1) evidences the actual orthorhombic symmetry of the tested composite. Consequently, we use the arithmetic mean of the two shear wave velocities for the further evaluation of stiffness properties.

Stiffness properties as calculated according to Eqs. (3-4) are summarized in Table 2. The normal stiffness in thickness direction, C_{2222} , is considerably smaller than the normal stiffness in the plane of the board. The stiffness in extrusion direction, C_{1111} , in turn, is slightly larger than the one in the perpendicular direction, C_{3333} . This orthotropic behavior can be explained by microstructural properties of the micro-heterogeneous composite material. Bagasse fibers are stiffer than the polypropylene matrix. Since bagasse fibers are predominantly oriented in extrusion direction, the highest stiffness values are observed in this direction.

The shear stiffness in the plane of the board, $C_{1313} = G_{13}$, is larger than the shear stiffnesses in the out-of-plane directions, where $C_{2323} = G_{23}$ is smaller than $C_{1212} = G_{12}$. This is consistent with the microstructural morphology described before.

3.2 Mechanical testing

Representative stress-strain curves for three orthogonal directions are presented in Figs. 3-5 (left), together with the evolution of strains over time (solid lines in the right-hand images) and the creep strain rate during the holding phase (dashed lines in the right-hand images).

The pronounced creep activity of the material results in non-linear stress paths even during loading (Figs. 3-5). Deformation measurements taken during the constant load levels quantify the creep activity in different material directions (see right-hand images in Figs. 3-5). In plane directions x_1 and x_3 exhibit a similar mechanical performance, while a considerably more compliant behavior was measured in the out-of-plane direction x_2 . As expected, creep deformations are increasing with increasing stress levels. Consequently, also strain rates (images on the right-hand side in Figs. 3-5) increase with increasing stresses.

Characteristic creep times τ_i for the different material directions and for three different load levels are summarized in Table 3. In each material direction and for the corresponding three stress levels, the use of three characteristic creep times in Eq. (5) yielded values smaller than the tolerated threshold value of $TOL = 10^{-7}$, according to the minimization process in Eq. (6).

Interestingly for all material directions, normalized strains $\varepsilon^{creep}/\sigma_0$ during the first and second load level are similar, which is also expressed by comparable characteristic creep times (cf. Table 3). This indicates viscoelastic material behavior up to the corresponding load levels. On the contrary, creep strains were considerably higher during the third load plateau, which might indicate plastic deformations in addition to creep.

Characteristic creep times were highest in x_2 -direction (thickness direction) and smallest in x_1 -direction (extrusion direction), see Table 3. This anisotropic (time-dependent) behavior can be explained by microstructural properties of the micro-heterogeneous composite

material. The time-dependent behavior of the bagasse fiber-polypropylene composite mainly stems from the polypropylene matrix, while bagasse fibers are significantly less creep active. Because of constraints during extrusion, bagasse fibers predominantly orient themselves in extrusion x_1 -direction, see Fig. 1(a) [19]. Constraints in x_2 -direction (thickness direction) are more pronounced than in x_3 -direction (in-plane direction), and this makes it least likely that bagasse fibers are oriented in x_2 -direction (thickness direction), see Fig. 1(b). Consequently, the visco-elastic behavior of polypropylene exhibits the strongest effect in x_2 -direction, followed by the x_3 -direction, and rendering the x_1 -direction the least creep active material direction.

A linear approximation of a specific section of the loading path, as often proposed by standards, does not yield elastic material properties. However, elastic properties of such a material can be determined under the assumption of an elastic immediate response when unloading. As for determination of Young's moduli, unloading branches were divided into equal strain increments of 5×10^{-5} , always starting from the end of each stress level. Corresponding results are illustrated in Figs. 6-8, where the average values of elastic modulus in three orthogonal directions, at different unloading strain increments, are shown for different load levels.

Figs. 6-8 indicate a minor dependence of the unloading stiffness on the size of the unloading strain increment, but larger moduli are observed for higher load levels. The latter result can be explained by the creep activity right before unloading. Upon *marginal* unloading, creep deformations will still result in a progressive shortening of the specimen, while spontaneous elastic deformation will result in an elongation of the specimen. Creep-related shortening counteracts the elasticity-related elongation such that unloading elongations are underestimated, and this results in an overestimated stiffness. This effect is

particularly pronounced in thickness direction x_2 , where the unloading stiffness determined by unloading from the second stress plateau is considerably larger than the one determined by unloading from the first stress plateau. In contrast to this observation, a significant increase of the unloading stiffness in in-plane-directions x_1 and x_2 , is only found when comparing results related to the second and the third stress plateau.

From a more quantitative standpoint, the aforementioned creep-induced error in the determination of the elastic properties relates to the ratio of creep and strain evolution times according to Eqs. (5-8): This creep-induced error goes to zero if the deformation time, T_{def} , is considerably larger than the highest characteristic creep time, T_{creep} . In Table 4, the corresponding values are summarized for the different material orientations and load levels. The factor between the deformation time and the characteristic creep time was the highest at the end of the first load level, while it decreased for higher loads. Consistent with the characteristic creep times, factors were highest in x_1 - and x_3 -direction, while lower values were calculated for the thickness direction x_2 . The longitudinal and in-plane transverse moduli E_1 and E_3 , determined at stress levels 1 and 2 differed only very little from each other (see Figs. 6-8), with the lowest corresponding T_{def}/T_{creep} ratio being as small as 3.8 (Table 4). Hence, such a ratio magnitude can be regarded as sufficiently large for virtually excluding creep-induced error in unloading modulus-based elasticity determination. The aforementioned value of 3.8 is also comparable to the T_{def}/T_{creep} ratio characterizing the situation of the first unloading process in x_2 direction. Consequently, the corresponding modulus E_2 can also be considered as elastic.

We summarize that the instantaneous unloading stiffnesses determined from unloading processes at the end of stress level 1, represent the elastic properties of the material. In

terms of Young's moduli, they are: $E_1=3.68 (\pm 0.80)$ GPa, $E_2=1.44 (\pm 0.20)$ GPa, and $E_3=2.79 (\pm 0.35)$ GPa. The largest elastic stiffness is E_1 , which refers to the extrusion direction, followed by the in-plane stiffness E_3 in direction normal to the extrusion direction. The smallest stiffness is given in out-of-plane direction, i.e. E_2 . Summarizing, results from mechanical testing are consistent with results from ultrasonic testing.

3.3 Quantification of Poisson's ratios and off-diagonal stiffness tensor components from combined ultrasonic and quasi-static tests

A material with orthorhombic symmetry exhibits nine independent elastic constants. Given that we have gained access to six stiffness tensor components via ultrasonic characterization and to three Young's moduli via quasi-static unloading, a complete characterization of the material has been accomplished. Therefore, it is possible to quantify, based on linear elasticity of orthotropic materials, numerical values of six Poisson's ratios and of three off-diagonal stiffness tensor components. The latter show up in the Kelvin-Mandel representation [22-24] of the stiffness tensor referring to the principal material directions,

$$[C] = \begin{bmatrix} C_{1111} & C_{1122} & C_{1133} & 0 & 0 & 0 \\ C_{2211} & C_{2222} & C_{2233} & 0 & 0 & 0 \\ C_{3311} & C_{3322} & C_{3333} & 0 & 0 & 0 \\ 0 & 0 & 0 & 2C_{2323} & 0 & 0 \\ 0 & 0 & 0 & 0 & 2C_{1313} & 0 \\ 0 & 0 & 0 & 0 & 0 & 2C_{1212} \end{bmatrix} = \begin{bmatrix} C_{1111} & C_{1122} & C_{1133} & 0 & 0 & 0 \\ C_{1122} & C_{2222} & C_{2233} & 0 & 0 & 0 \\ C_{1133} & C_{2233} & C_{3333} & 0 & 0 & 0 \\ 0 & 0 & 0 & 2G_{23} & 0 & 0 \\ 0 & 0 & 0 & 0 & 2G_{13} & 0 \\ 0 & 0 & 0 & 0 & 0 & 2G_{12} \end{bmatrix}, \quad (9)$$

with shear moduli G_{ij} . The compliance tensor $[D]$ of the orthotropic material is the inverse of the stiffness tensor, i.e. $[D] = [C]^{-1}$, and the corresponding matrix-representation of $[D]$ reads as

$$[D] = \begin{bmatrix} D_{1111} & D_{1122} & D_{1133} & 0 & 0 & 0 \\ D_{1122} & D_{2222} & D_{2233} & 0 & 0 & 0 \\ D_{1133} & D_{2233} & D_{3333} & 0 & 0 & 0 \\ 0 & 0 & 0 & 2D_{2323} & 0 & 0 \\ 0 & 0 & 0 & 0 & 2D_{1313} & 0 \\ 0 & 0 & 0 & 0 & 0 & 2D_{1212} \end{bmatrix} = \begin{bmatrix} \frac{1}{E_1} & -\frac{\nu_{12}}{E_2} & -\frac{\nu_{13}}{E_3} & 0 & 0 & 0 \\ -\frac{\nu_{21}}{E_1} & \frac{1}{E_2} & -\frac{\nu_{23}}{E_3} & 0 & 0 & 0 \\ -\frac{\nu_{31}}{E_1} & -\frac{\nu_{32}}{E_2} & \frac{1}{E_3} & 0 & 0 & 0 \\ 0 & 0 & 0 & \frac{1}{2G_{23}} & 0 & 0 \\ 0 & 0 & 0 & 0 & \frac{1}{2G_{13}} & 0 \\ 0 & 0 & 0 & 0 & 0 & \frac{1}{2G_{12}} \end{bmatrix} \quad (10)$$

with Young's moduli E_i and Poisson's ratios ν_{ij} , where subscripts i and j refer to directions of lateral strain and applied stress respectively. Considering the orthorhombic symmetry of the compliance tensor, there are nine independent elastic components including three independent Poisson's ratios. The remaining three Poisson's ratios are dependent quantities and satisfy the conditions $\nu_{ij}/E_j = \nu_{ji}/E_i$. *Isotropic* elastic materials exhibit just one Poisson's ratio and it is bounded between -1 and 0.5. *Anisotropic* materials, in turn, exhibit several Poisson's ratios without theoretical bounds, as long as the strain energy density is positive definite [35].

Consideration of Eqs. (9-10) together with the condition $[D] = [C]^{-1}$ yields the following three equations for the determination of the Poisson's ratios ν_{21} , ν_{31} , and ν_{32} as functions (i) of the normal stiffness tensor components C_{1111} , C_{2222} , and C_{3333} , as well as (ii) of the Young's moduli E_1 , E_2 , and E_3 , see also Eqs. (23-29) in [20]

$$\nu_{21} = \frac{1}{2\sqrt{2}E_2E_3} \sqrt{\frac{n_{21}}{C_{1111}C_{2222}}}, \quad (11)$$

$$\nu_{31} = \frac{1}{2\sqrt{2}E_2E_3} \sqrt{\frac{n_{31}}{C_{1111}C_{3333}}}, \quad (12)$$

$$\nu_{32} = \frac{n_{32}}{f g_{12} g_{32}} \sqrt{n_{21} n_{31} \frac{C_{2222}}{C_{3333}}}, \quad (13)$$

where

$$n_{21} = n_{12} - h, \quad (14)$$

$$n_{31} = c_3^2 - 2E_3c_3d_{31} + E_3^2e_{31} - h, \quad (15)$$

$$n_{32} = c_3^2 - 2E_3c_3d_{32} + E_3^2e_{32} + h, \quad (16)$$

and

$$f = -16c_1c_2E_3^2, \quad (17)$$

$$g_{12} = c_3 - E_3d_{12}, \quad (18)$$

$$g_{32} = c_3 - E_3d_{32}, \quad (19)$$

$$n_{12} = c_3^2 - 2E_3c_3d_{21} + E_3^2e_{21}, \quad (20)$$

$$h = \sqrt{fg_{12}^2 + n_{12}^2}, \quad (21)$$

with

$$e_{21} = c_2^2 - 2E_2c_2b_2 + E_2^2a_2^2, \quad (22)$$

$$e_{31} = c_2^2 - 2E_2c_2a_1 + E_2^2a_2^2, \quad (23)$$

$$e_{32} = c_2^2 - 2E_2c_2a_2 + E_2^2a_2b_1, \quad (24)$$

$$d_{12} = c_2 - E_2a_2, \quad (25)$$

$$d_{21} = c_2 + E_2a_1, \quad (26)$$

$$d_{31} = c_2 + E_1E_2 - 3c_1, \quad (27)$$

$$d_{32} = c_2 + E_1E_2 - c_1, \quad (28)$$

$$c_1 = C_{1111}E_2, \quad c_2 = C_{2222}E_1, \quad c_3 = C_{3333}E_1E_2, \quad (29)$$

$$a_1 = E_1 + C_{1111}, \quad a_2 = E_1 - C_{1111},$$

$$b_1 = E_1 + 3C_{1111}, \quad b_2 = E_1 - 3C_{1111}. \quad (30)$$

Inserting stiffness tensor components as measured by means of ultrasonic testing as well as Young's moduli as measured by means of mechanical testing into Eqs. (11-13) yields Poisson's ratios and off-diagonal stiffness tensor components of the orthotropic material as

given in Table 5. The determined Poisson's ratio values lie between 0.230 and 0.722. Corresponding off-diagonal stiffness tensor components range between 3.479 and 4.273 GPa. For the pair of in-plane Poisson's ratios ν_{31} and ν_{13} , values close to each other are found, while the other two pairs of Poisson's ratios showed larger differences. This is a result of the anisotropy of the material, which is most pronounced between the in-plane and out-of plane directions.

Considering the statistical variation of stiffnesses and Young's moduli obtained from ultrasonic and quasi-static testing, respectively, allows for quantifying the statistical variations of Poisson's ratios determined by the above described approach, see Table 5. Notably, the out-of plane Poisson's ratios are less sensitive than the in-plane Poisson's ratios, and this can be explained by the variability of the Young's modulus E_1 , which is significantly larger than the variability of E_2 and E_3 .

4. Conclusions

The aim of this research was to characterize elastic properties for an orthotropic bagasse fiber-polypropylene composite by combining ultrasonics and mechanical testing. The following conclusions can be drawn from the present study:

- The stiffest material behavior was measured in extrusion direction, both in ultrasonics and quasi-static tests. This indicates that bagasse fibers are predominantly oriented in this direction.
- The differences of shear wave velocities in three pairs of orthogonal directions were found to be very small, evidencing orthorhombic symmetry of the studied composite.

- Significant creep deformations were observed in compression tests. They were particularly significant in the thickness direction x_2 , where the impact of the polypropylene matrix is strongest because it is least likely that bagasse fibers are aligned with the x_2 -direction.
- In order to obtain realistic values for Young's moduli, creep deformations must be excluded from the analysis. Therefore, unloading stiffness was determined after a sufficiently long stress level, whereby the latter was small enough such that creep deformations had practically faded out before unloading took place.
- As a novel contribution, Poisson's ratios of the orthotropic material and off-diagonal stiffness tensor components were calculated by combining ultrasonics and quasi-static test data.

5. References

- [1] Luz SM, Goncalves AR and Del'Arco AP. Mechanical behavior and microstructural analysis of sugarcane bagasse fibers reinforced polypropylene composites, *Compos Part A-Appl S* 2007;38:1455–1461.
- [2] Moubarik A, Grimi N, Boussetta N. Structural and thermal characterization of Moroccan sugar cane bagasse cellulose fibers and their applications as a reinforcing agent in low density polyethylene, *Compos Part B-Eng* 2013;52:233–238.
- [3] Yan L, Kasal B, Huang L, A review of recent research on the use of cellulosic fibres, their fibre fabric reinforced cementitious, geo-polymer and polymer composites in civil engineering, *Compos Part B-Eng* 2016;92:94–132.
- [4] Verma D, Gope PC, Maheshwari MK, Sharma RK. Bagasse Fiber Composites – A Review. *J Mater Env Sci* 2012;3(6):1079–1092.

- [5] Xue Y, Veazie DR, Glinsey C, Horstemeyer MF, Rowell RM, Environmental effects on the mechanical and thermomechanical properties of aspen fiber–polypropylene composites, *Compos Part B-Eng* 2007;38(2):152–158.
- [6] Cai ZH, Ross RJ. Mechanical properties of wood-based composite materials. In: *Wood handbook*, Forest Products Laboratory, 2011. p.12.1–12.12.
- [7] Haiar KJ. Performance and design of prototype wood-plastic composite sections. MSc thesis, Washington State University, 2000.
- [8] Odell J. Wood plastic composite sill plate for continuous anchorage of shear walls in light frame wood structures. MSc thesis, Washington State University, 2008.
- [9] Arrakhiz FZ, Malha M, Bouhfid R, Benmoussa K, Qaiss A. Tensile, flexural and torsional properties of chemically treated alfa, coir and bagasse reinforced polypropylene, *Compos Part B-Eng* 2013;47:35–41.
- [10] Ashori A, Nourbakhsh A. Polypropylene Cellulose-Based Composites: The Effect of Bagasse Reinforcement and Polybutadiene Isocyanate Treatment on the Mechanical Properties, *J Appl Polym Sci* 2009;111:1684–1689.
- [11] Nourbakhsh A, Kouhpayehzadeh M. Mechanical properties and water absorption of fiber-reinforced polypropylene composites prepared by bagasse and beech fiber, *J Appl Polym Sci* 2009;114:653–657.
- [12] Cao Y, Goda K, Shibata S. Development and mechanical properties of bagasse fiber reinforced composites, *Adv Compos Mater* 2007;16(4):283–298.
- [13] Cerqueira EF, Baptista CARP, Mulinari DR. Mechanical behavior of polypropylene reinforced sugarcane bagasse fibers composites, *Procedia Eng* 2011;10:2046–2051.
- [14] Vázquez A, Domínguez VA, Kenny JM. Bagasse Fiber-Polypropylene Based Composites, *J Thermoplast Compos* 1999;12:477–497.

- [15] Samariha A, Bastani A, Nemati M, Kiaei M, Nosrati H, Farsi M. Investigation of the mechanical properties of bagasse flour/polypropylene composites, *Mech Compos Mater* 2013;49(4):447–454.
- [16] Cao Y, Shibata S, Fukumoto I. Mechanical properties of biodegradable composites reinforced with bagasse fibre before and after alkali treatments, *Compos Part A-Appl S* 2006;37:423–429.
- [17] Rodrigues EF, Maia TF and Mulinari DR. Tensile strength of polyester resin reinforced sugarcane bagasse fibers modified by esterification. *Procedia Eng* 2011;10: 2348–2352.
- [18] Muszynski L. Imaging Wood Plastic Composites (WPCs): X-Ray computed tomography, a few other promising techniques, and why we should pay attention, *Bioresources* 2009;4(3):1210–1221.
- [19] Prapathanssiou TD, Guell DC. *Flow Induced Alignment in Composite Materials*, Woodhead Pub., England, 1997.
- [20] Kohlhauser C, Hellmich C. Determination of Poisson's ratios in isotropic, and orthotropic materials by means of combined ultrasonic-mechanical testing of normal stiffnesses: application to metals and wood, *Eur J Mech A-Solids* 2012;33:82–98.
- [21] Kriz R, Stinchcomb W. Elastic moduli of transversely isotropic graphite fibers and their composites. *Exp Mech* 1979;19(2):41–49.
- [22] Walpole LJ. Fourth-Rank Tensors of the Thirty-Two Crystal Classes: Multiplication Tables. *Proc R Soc Lond A* 1984;391:149–179.
- [23] Mehrabadi MM, Cowin SC. Eigentensors of linear anisotropic elastic materials, *Q J Mech Appl Math* 1990;43:15–41.
- [24] Helnwein P. Some remarks on the compressed matrix representation of symmetric second-order and fourth-order tensors, *Comput Method Appl M* 2001;190(22-23):2753–2770.

- [25] ASTM E11-95, Standard Specification for Wire Cloth and Sieves for Testing Purposes, ASTM International, West Conshohocken, PA, 2001.
- [26] Zaoui A. Continuum micromechanics: survey. *J Eng Mechan (ASCE)* 2002;128(8):808–816.
- [27] Drugan WJ, Willis JR. A micromechanics-based nonlocal constitutive equation and estimates of representative volume element size for elastic composites, *J Mech Phys Solids* 1996;44:497–524.
- [28] Kohlhauser C, Hellmich C. Ultrasonic contact pulse transmission for elastic wave velocity and stiffness determination: Influence of specimen geometry and porosity, *Eng Struct* 2013;47:115–133.
- [29] Carcione J. Wave Fields in Real Media: Wave Propagation in Anisotropic, Anelastic and Porous Media. In: *Handbook of Geophysical Exploration – Seismic exploration*, first ed., vol. 31. Pergamon Elsevier Science Ltd., Oxford, United Kingdom, 2001.
- [30] Coussy O. Poromechanics. John Wiley & Sons, Ltd, England, 2004.
- [31] Luczynski KW, Brynk T, Ostrowska B, Swieszkowski W, Reihnsner R, Hellmich C. Consistent quasistatic and acoustic elasticity determination of poly-L-lactide-based rapid-prototyped tissue engineering scaffolds. *J Biomed Mater Res A* 2013;101A:138–144.
- [32] Luczynski KW, Steiger-Thirsfeld A, Bernardi J, Eberhardsteiner J, Hellmich C. Extracellular bone matrix exhibits hardening elastoplasticity and more than double cortical strength: Evidence from homogeneous compression of non-tapered single micron-sized pillars welded to a rigid substrate. *J Mech Behav Biomed Mat* 2015; doi:10.1016/j.jmbbm.2015.03.001.
- [33] Lakes RS. Viscoelastic solids. CRC press LLC, 1999.
- [34] Auriault JL, Boutin C, Geindreau C. Homogenization of Coupled Phenomena in Heterogenous Media. Wiley-ISTE, 2010.

- [35] Ting, TCT, Chen T. Poisson's ratio for anisotropic elastic materials can have no bounds,
Q J Mech Appl Math 2005;58(1):73–82.

ACCEPTED MANUSCRIPT

List of figure captions

Figure 1: Optical micrograph: (a) cross-section parallel to the extrusion direction (i.e. x_1), and (b) cross-section normal to the extrusion direction; the lighter colored phase is the bagasse fibers and the darker colored phase is the matrix.

Figure 2: I-shaped profile from which specimens for ultrasonic and mechanical testing were cut out, see the dashed lines; and orientation of Cartesian x_1, x_2, x_3 -coordinate axes.

Figure 3: Left: Loading-unloading stress-strain curve; right: normal strain and creep strain rate in extrusion direction x_1 .

Figure 4: Left: Loading-unloading stress-strain curve; right: normal strain and creep strain rate in direction x_2 (out-of-plane and normal to extrusion direction).

Figure 5: Left: Loading-unloading stress-strain curve; right: normal strain and creep strain rate in direction x_3 (in-plane and normal to extrusion direction)

Figure 6: Elastic modulus computed for different unloading displacement increments at various stress levels in direction 1 (extrusion direction, i.e. x_1).

Figure 7: Elastic modulus computed for different unloading displacement increments at various stress levels in direction 2 (i.e. x_2).

Figure 8: Elastic modulus computed for different unloading displacement increments at various stress levels in direction 3 (i.e. x_3).

Table 1: Average values and standard deviations (given in brackets) of measured ultrasonic wave travel times t , wave velocities V computed according to Eq. (2), and wavelengths λ computed according to Eq. (1).

travel time of ultrasound waves (in μs)								
t_{11}	t_{22}	t_{33}	t_{12}	t_{21}	t_{13}	t_{31}	t_{23}	t_{32}
19.69 (± 0.78)	7.10 (± 1.10)	5.44 (± 1.16)	43.22 (± 1.97)	11.50 (± 0.35)	39.84 (± 1.02)	10.08 (± 0.51)	12.04 (± 2.09)	12.26 (± 2.37)
wave velocities (in km s^{-1})								
V_{11}	V_{22}	V_{33}	V_{12}	V_{21}	V_{13}	V_{31}	V_{23}	V_{32}
2.59 (± 0.06)	1.83 (± 0.11)	2.39 (± 0.14)	1.18 (± 0.05)	1.13 (± 0.03)	1.28 (± 0.34)	1.29 (± 0.48)	1.08 (± 0.09)	1.06 (± 0.02)
wavelength (in mm)								
λ_{11}	λ_{22}	λ_{33}	λ_{12}	λ_{21}	λ_{13}	λ_{31}	λ_{23}	λ_{32}
25.9	18.3	23.9	4.72	4.54	5.11	5.15	4.32	4.24

Table 2: Mean values and standard deviation (given in brackets) of stiffness tensor components derived from ultrasonics testing according to Eqs. (3-4).

stiffness tensor component	mean value (in GPa)	standard deviation (in GPa)
C_{1111}	7.39	± 0.37
C_{2222}	3.68	± 0.73
C_{3333}	6.29	± 0.26
$C_{1313}=G_{13}$	1.82	± 0.11
$C_{1212}=G_{12}$	1.47	± 0.09
$C_{2323}=G_{23}$	1.26	± 0.08

Table 3: Characteristic creep times τ_i and normalized amplitudes A_i determined according to Eq. (5).

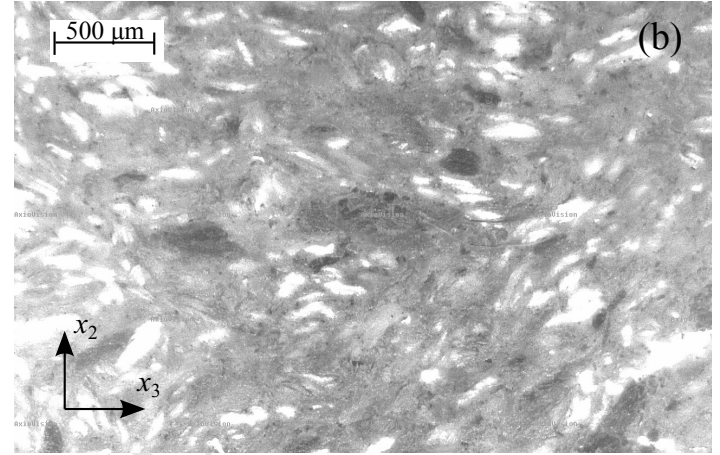
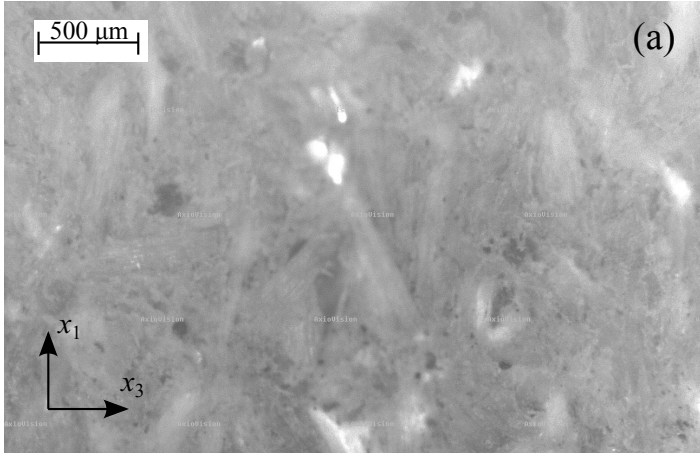
	direction x_1 (in-plane parallel to extrusion direction)	direction x_2 (out-of-plane and normal to extrusion direction)	direction x_3 (in-plane and normal to extrusion direction)
1 st holding	$A_1 = 1.810 \cdot 10^{-5}$	$A_1 = 7.050 \cdot 10^{-5}$	$A_1 = 1.916 \cdot 10^{-5}$
	$A_2 = 3.824 \cdot 10^{-5}$	$A_2 = 2.180 \cdot 10^{-4}$	$A_2 = 4.283 \cdot 10^{-5}$
	$A_3 = 8.823 \cdot 10^{-5}$	$A_3 = 5.612 \cdot 10^{-4}$	$A_3 = 1.032 \cdot 10^{-4}$
	$\tau_1 = 4.21$ s	$\tau_1 = 8.44$ s	$\tau_1 = 4.64$ s
	$\tau_2 = 29.24$ s	$\tau_2 = 56.68$ s	$\tau_2 = 30.56$ s
	$\tau_3 = 273.70$ s	$\tau_3 = 551.8$ s	$\tau_3 = 236.30$ s
2 nd holding	$A_1 = 2.243 \cdot 10^{-5}$	$A_1 = 1.175 \cdot 10^{-4}$	$A_1 = 1.710 \cdot 10^{-5}$
	$A_2 = 3.069 \cdot 10^{-5}$	$A_2 = 3.195 \cdot 10^{-4}$	$A_2 = 3.264 \cdot 10^{-5}$
	$A_3 = 8.680 \cdot 10^{-5}$	$A_3 = 8.772 \cdot 10^{-4}$	$A_3 = 1.046 \cdot 10^{-4}$
	$\tau_1 = 12.61$ s	$\tau_1 = 21.18$ s	$\tau_1 = 11.23$ s
	$\tau_2 = 76.69$ s	$\tau_2 = 90.66$ s	$\tau_2 = 56.69$ s
	$\tau_3 = 542.20$ s	$\tau_3 = 614.70$ s	$\tau_3 = 480.50$ s
3 rd holding	$A_1 = 1.459 \cdot 10^{-5}$	$A_1 = 6.463 \cdot 10^{-5}$	$A_1 = 3.615 \cdot 10^{-5}$
	$A_2 = 5.781 \cdot 10^{-5}$	$A_2 = 2.531 \cdot 10^{-4}$	$A_2 = 7.788 \cdot 10^{-5}$
	$A_3 = 2.083 \cdot 10^{-4}$	$A_3 = 7.719 \cdot 10^{-4}$	$A_3 = 2.671 \cdot 10^{-5}$
	$\tau_1 = 16.63$ s	$\tau_1 = 28.17$ s	$\tau_1 = 18.61$ s
	$\tau_2 = 84.09$ s	$\tau_2 = 107.10$ s	$\tau_2 = 94.15$ s
	$\tau_3 = 653.20$ s	$\tau_3 = 713.60$ s	$\tau_3 = 788.00$ s

Table 4: Characteristic times T_{def} according to Eq. (8) and T_{creep} according to Eq. (7).

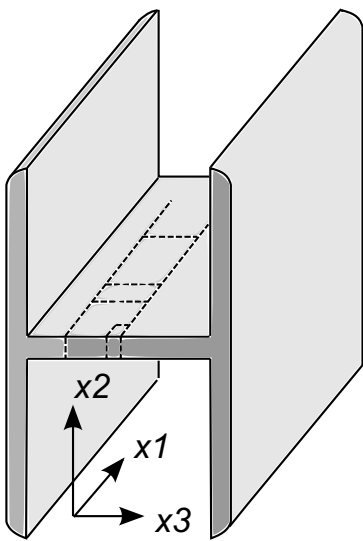
		direction x_1 (in-plane parallel to extrusion direction)	direction x_2 (out-of-plane and normal to extrusion direction)	direction x_3 (in-plane and normal to extrusion direction)
	T_{creep} (in s)	274	552	236
1 st unloading	T_{def} (in s)	3751	1917	3176
	T_{def}/T_{creep} (-)	13.7	3.5	13.5
	T_{creep} (in s)	542	615	481
2 nd unloading	T_{def} (in s)	2082	1793	1973
	T_{def}/T_{creep} (-)	3.8	2.9	4.1
	T_{creep} (in s)	653	714	788
3 rd unloading	T_{def} (in s)	1457	1568	1571
	T_{def}/T_{creep} (-)	2.2	2.2	2.0

Table 5: Poisson's ratios obtained from combined ultrasonics ($C_{1111}=7.39$ GPa , $C_{2222}=3.68$ GPa, $C_{3333}=6.29$ GPa) and quasi-static mechanical tests ($E_1=3.68$ GPa, $E_2=1.44$ GPa, $E_3=2.79$ GPa).

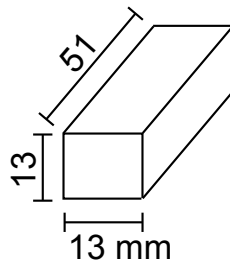
	Poisson's ratios (-)			off-diagonal stiffness tensor components (in GPa)			
	mean	mean-std	mean+std		mean	mean-std	mean+std
ν_{21}	0.678	0.606	0.791	C_{1122}	3.554	3.198	3.792
ν_{12}	0.265	0.261	0.289	C_{1133}	4.273	4.659	3.572
ν_{31}	0.304	0.473	0.079	C_{2233}	3.479	2.985	3.864
ν_{13}	0.230	0.401	0.055				
ν_{32}	0.373	0.293	0.432				
ν_{23}	0.722	0.577	0.829				



ACCEPTED MANUSCRIPT



Ultrasound



Mechanical testing

direction 1

direction 2

direction 3

